JOURNAL OF GEOPHYSICAL RESEARCH, VOL. 100, NO. C10, PAGES 20,729–20,743, OCTOBER 15, 1995

Glimpses of a wave boundary layer

J. H. Trowbridge

Woods Hole Oceanographic Institution, Woods Hole, Massachusetts

Y. C. Agrawal

Sequoia Scientific, Incorporated, Mercer Island, Washington

Abstract. Measurements obtained with a profiling laser–Doppler velocimeter reveal the vertical structure of velocity in a wave boundary layer over a sand beach during two periods of approximately stationary forcing, each with a duration of several hours. The measurements indicate clearly the reduction in variance and the increase in phase, relative to the overlying flow, that are expected in an oscillatory boundary layer. The measurements also indicate a distortion of the mean alongshore velocity within the wave boundary layer, which has previously been predicted theoretically and observed in laboratory experiments. The thickness and structure of the boundary layer are approximately consistent with computations based on an existing eddy viscosity model, and model–based best fit estimates of bottom roughness are approximately consistent with existing semiempirical descriptions of wave–formed sand ripples.

1. Introduction

Wind–generated ocean surface waves produce a thin boundary layer at the seafloor, where the flow is rotational and frictional effects cannot be neglected. Wave boundary layers are important in shallow coastal regions because they control entrainment of sediment from the bottom and because they can be the site of substantial energy dissipation. In the simplest case, in which the motion is laminar and the bottom is smooth and fixed, the flow within the boundary layer is described by the classical Stokes solution [e.g., *Batchelor*, 1967]. Under conditions more typical of the coastal ocean, in which the bottom is rough and erodible and the motion may be turbulent, there is no generally accepted theory, so that the structure of the boundary layer is a topic of current research.

Most of the existing information about wave boundary layers comes from laboratory measurements and mathematical models. Laboratory experiments have addressed primarily the idealized case of monochromatic oscillatory flows over fixed smooth or artificially roughened boundaries [*Jonsson and Carlsen*, 1976; *Hino et al.*, 1983; *Kemp and Simons*, 1982, 1983; *Sleath*, 1987; *Jensen et al.*, 1989], and semiempirical mathematical models have also been directed primarily toward this case [e.g., *Kajiura*, 1968; *Smith*, 1977; *Grant and Madsen*, 1979; *Brevik*, 1981]. A few laboratory measurements in oscillatory flows over rippled bottoms have been reported [*DuToit and Sleath*, 1981; *Sato et al.*, 1984], and mathematical models of flows over rippled bottoms have been developed for small [*Sleath*, 1974; *Hara and Mei*, 1989] and large [*Longuet–Higgins*, 1981] Reynolds numbers. A few laboratory measurement programs have addressed some of the features of oscillatory flows over sand beds under intense conditions in which sand ripples cannot form (sheet flow conditions) [*DuToit and Sleath*, 1981; *Sawamoto and Yamashita*, 1986; *Dick and Sleath*, 1991].

Oceanic measurements in wave boundary layers have been rare. Measurements of backscattered acoustical intensity with fine vertical resolution have in some cases indicated an abrupt change in structure several centimeters above bottom, suggesting the presence of a wave boundary layer [e.g., *Hay and Sheng*, 1992]. *Conley and Inman* [1992] identified qualitative near–bottom flow structures under waves based on video images and hot-film measurements. *Agrawal and Aubrey* [1992] obtained profile measurements with a laser–Doppler velocimeter over a rippled bed under conditions of weak forcing, in which the wave boundary layer was transitionally turbulent. To our knowledge, the vertical structure of velocity in a wave boundary layer under conditions of moderate or strong forcing has not previously been resolved in oceanic measurements.

In this paper we report measurements obtained with a profiling laser–Doppler velocimeter in an oceanic wave boundary layer. The primary objective of the measurements was to observe the reduction in amplitude and the phase lead, relative to the overlying flow, that are characteristic of an oscillatory boundary layer [e.g., *Batchelor*, 1967] and to compare these features with computations based on existing quantitative models. We also hoped to observe the distortion of the mean

Paper number 95JC02131.
0148-0227/95/95JC-02131$05.00

flow within the wave boundary layer that has been predicted theoretically [e.g., *Grant and Madsen*, 1979] and observed in laboratory experiments [e.g., *Kemp and Simons*, 1982, 1983]. In the following we first describe the measurements (section 2) and the analysis (section 3). We then present and discuss the results (sections 4 and 5) and summarize conclusions (section 6).

2. Measurements

2.1. Instrumentation

The primary instrument was a two–axis laser–Doppler velocimeter (LDV) with a 100–mW gallium–aluminum laser, manufactured by Quest, Integrated, Incorporated, located in Kent, Washington. This instrument is a fiber–optic backscatter sensor that "looks" downward to provide an unobstructed measurement of two horizontal components of velocity. The sensor head is cylindrical, with a diameter of 3 cm. To reduce the length of the optical path in sediment–laden water, a water–filled, tapered, plastic "snout" was fixed to the end of the sensor head. The sensing volume was 1 cm away from the end of the snout, and it was approximately ellipsoidal in shape, with a major (vertical) axis of approximately 1 mm and a minor (horizontal) axis of approximately 0.15 mm. The internal processor determined whether each measurement was valid or not, using preset criteria based on the quality of the raw optical signal.

Secondary instruments were a benthic acoustic stress sensor (BASS), a pressure sensor, and a video camera. BASS, manufactured by A. J. Williams of the Woods Hole Oceanographic Institution, is an acoustic travel time current meter, in which four acoustic paths with lengths of 15 cm occupy a sample volume [*Williams et al.*, 1987]. The pressure sensor, manufactured by Synsym, Incorporated, located in Sunnyvale, California, is a rapid–response, strain–gauge device. The submersible video camera was manufactured by Deep Sea Power and Light, Incorporated, of San Diego, California.

We mounted the LDV, BASS, pressure sensor, and video camera on a tripod (Figure 1). The LDV was fixed to a mechanical profiling system that permitted measurements at a range of heights above bottom. The BASS, pressure sensor, and video camera were stationary. Control of the LDV profiling device and acquisition of LDV, BASS, and pressure data were accomplished by a Tattletale model 6 computer mounted on the tripod. External control of the system was possible through a hard–wired link to shore–based personal computers. The analog video images were hard–wired to shore and collected there.

The microprocessor controlling the LDV profiler was programmed to obtain sequential 90–s records at heights of 0.5, 1.0, 2.0, 4.0, 8.0 and 16.0 cm above a nominal bottom. The system recorded data in blocks of 12 such records (i.e., two records at each of 6 heights), so that each data block contained 18 min of data. The simultaneous sampling of the LDV and pressure sensor was at a rate of 25 Hz, and synchronized sampling of the BASS occurred at a rate of 10 Hz. A shore–based oper-

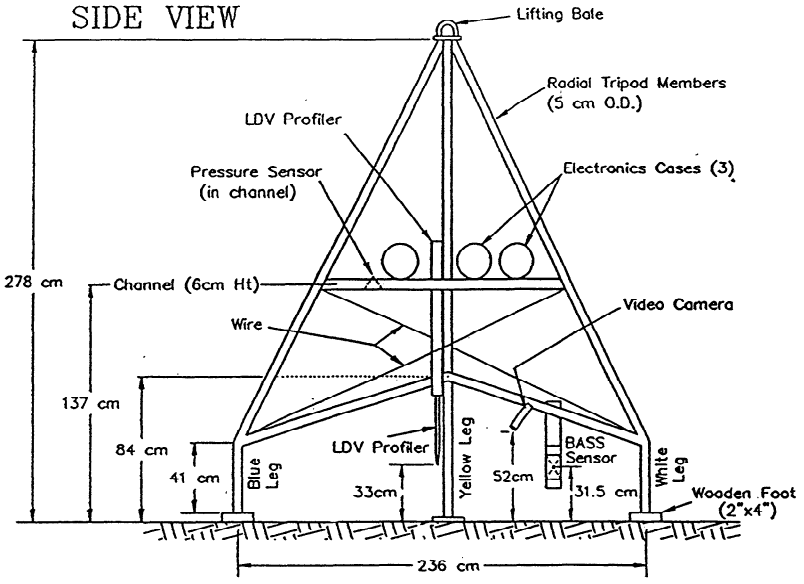

Figure 1. Diagram of the tripod and instrumentation. The laser-Doppler velocimeter (LDV), shown in its highest possible ("home") position, was mounted on a mechanical profiling system that permitted measurements at a range of heights above bottom. The benthic acoustic stress sensor (BASS), pressure sensor, and video camera were stationary. All heights of sensors here are relative to a hard bottom just beneath the tripod's wooden feet. The LDV sensing volume was 1 cm below the bottom of a water–filled "snout" or 32 cm above the hard bottom. During the actual experiment the heights of the sensors above the sand bottom were substantially different because scuba divers "worked" the feet into the sand during the deployment. The tripod legs are denoted by colors for convenience.

ator initiated the collection of each 18–min data block by means of a software command communicated by the hard–wired link to the tripod, so that data collection could be interrupted for the purpose of adjusting LDV parameters, including, in particular, the elevation with respect to the fixed tripod of the nominal bottom to which LDV elevations were referenced. We estimated the proper location of the nominal bottom by means of an operator–controlled procedure in which the LDV was moved slowly downward from its highest position until an exceptionally strong backscattered optical signal was encountered.

2.2. Deployment

The measurement site was the Field Research Facility (FRF) in Duck, North Carolina, operated by the U. S. Army Corps of Engineers Waterways Experiment Station [*Birkemeier et al.*, 1985]. FRF personnel deployed the tripod from an amphibious vehicle at a position approximately 610 m offshore of the FRF baseline and 56 m north of the FRF pier (Figure 2), where the water depth relative to National Geodetic Vertical Datum (NGVD) (in this case roughly equal to the mean water level) was approximately 6 m. The bottom at the location of the tripod was composed of well–sorted sand, with a mean diameter of roughly 200 μm [*Stauble*, 1992]. Scuba divers measured the tripod's orientation by means of a compass mounted on a temporary bracket well away from the magnetic interference of the tripod itself. We estimate that the uncertainty of this measurement is a few degrees. One of the two LDV axes was aligned as closely as we could determine with the orientation of the coastline, so that it measured alongshore velocity, and the other LDV axis was aligned in the cross–shore direction. Scuba divers also measured

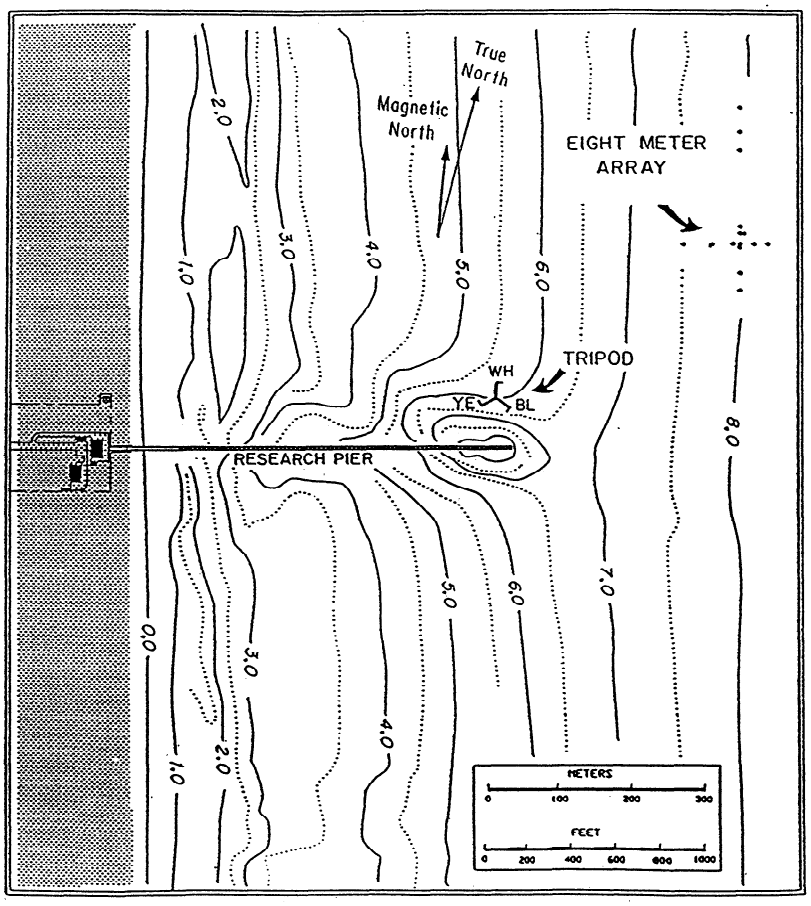

Figure 2. Map of the deployment site. Depth contours (in meters) are relative to National Geodetic Vertical Datum, which was approximately the same as the mean water level during the measurement period. The notations WH, YE, and BL denote the white, yellow, and blue legs of the tripod, respectively. The eight-meter array is a directional wave measurement array maintained by Field Research Facility (FRF) personnel. The tripod position (chosen before the deployment on the basis of an older map) was just inside a region of topographical perturbations apparently associated with the research pier. The measurements do not seem, however, to have been influenced strongly by local topographical effects. Cross–shore and alongshore, as used in the text, indicate directions perpendicular and parallel, respectively, to the coastline, rather than perpendicular and parallel to the local isobaths at the tripod. Diagram (exclusive of the tripod) is courtesy of FRF personnel.

the height above the local bottom of the BASS sensor and the LDV sensor (in its highest position).

The measurement period, from approximately noon on December 4, 1992, until approximately noon on December 6, 1992, consisted of two distinct parts (Figure 3). During the first, between approximately 1430 and 2200 hours on December 4, the mean velocity at the BASS (averaged over individual 18–min blocks) was shore–parallel and northward, with a magnitude of 5 to 10 cm s^{-1}. Surface waves were incident from the east–southeast, with a dominant frequency of approximately 0.11 Hz and a root–mean–square (rms) near–bottom velocity of approximately 10 cm s^{-1}. The sand bottom was clearly visible in the video images during all of this period, and wave–formed ripples were present, with relatively short crests, a wavelength of roughly 10 cm, and crests roughly perpendicular to the direction of wave propagation. During the second part of the measurement period, between approximately 1400 hours on December 5 and 1000 hours on December 6, the mean velocity was shore–parallel and southward, with a magnitude of 10 to 20 cm s^{-1}. Surface waves were incident from the east–northeast, with a dominant frequency of approximately 0.16 Hz and an rms velocity of some 30 cm s^{-1}. The bottom was not visible in video images during this period because of a large amount

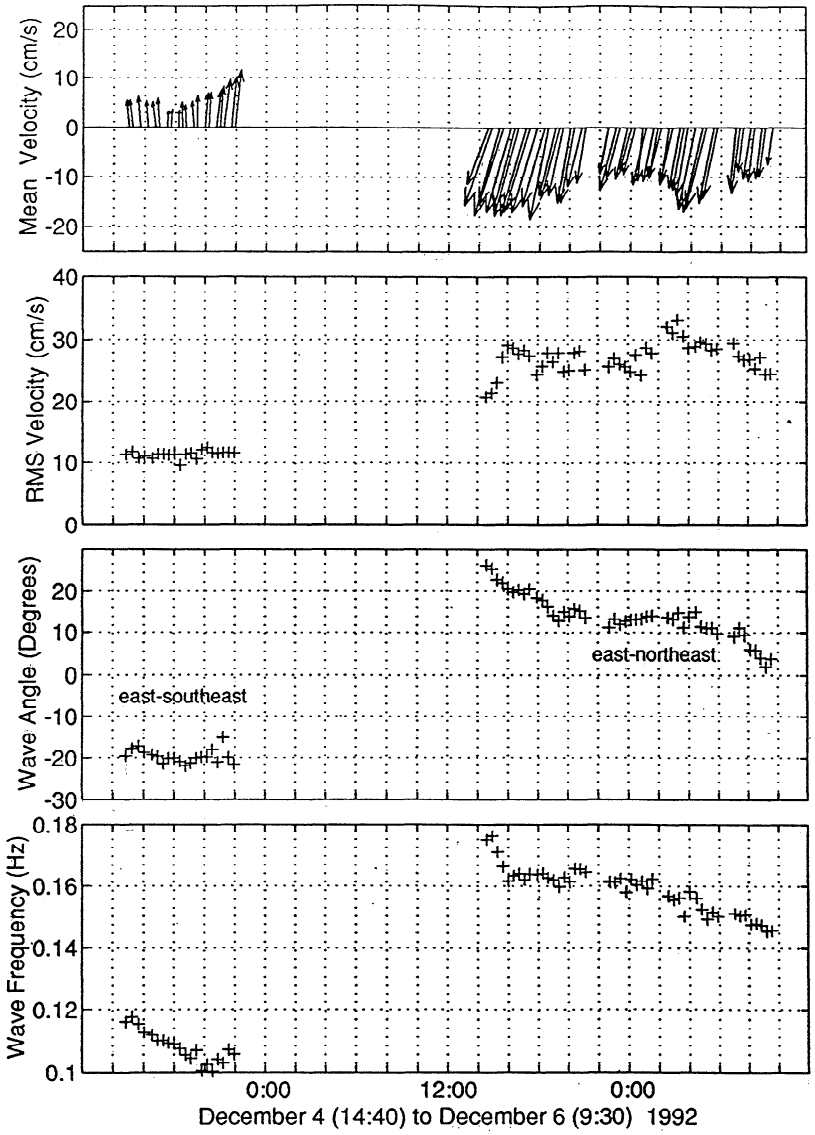

Figure 3. Wave and current conditions to BASS during the measurement period based on averages over the 12 90-s records in individual 18-min data blocks, (including from top to bottom) a stick plot of mean velocity; root–mean–square (rms) wave–induced velocity, equal to $(\sigma_u^2 + \sigma_v^2)^{1/2}$, where σ_u and σ_v are standard deviations of cross–shore and alongshore velocity, respectively; angle of wave incidence measured counterclockwise from shore–normal and estimated as the orientation of the principal axis of the velocity fluctuations; and mean frequency $\overline{f}$, defined by $\overline{f} = \int_0^{+\infty} fS(f)df / \int_0^{+\infty} S(f)df$, where f is frequency and S is the sum of spectra of cross–shore and alongshore velocity.

of suspended material. Just before recovery, however, the video images indicated wave-formed ripples with relatively short crests, a wavelength of approximately 10 cm, and crests approximately perpendicular to the direction of wave propagation, as before. The tripod was well outside of the surf zone during both parts of the measurement period. The gap between the first and second parts of the record (Figure 3) was devoted to off-loading data via the hard-wired link to shore-based personal computers.

During both parts of the measurement period, the direction of wave propagation was slightly inclined from shore-normal (Figure 3) and the energy of wave-induced velocity fluctuations was relatively narrowly distributed with respect to both frequency and direction. In particular, *Longuet-Higgins'* [1983] spectral width parameter ν^2, defined by

$$\nu^2 = \frac{\int_0^{+\infty}(f-\overline{f})^2 S(f)df}{\overline{f}^2 \int_0^{+\infty} S(f)df}, \quad (1)$$

was small (approximately 0.2 during the first part of the measurement period and 0.1 during the second). Here f is frequency, $S(f)$ is the sum of cross-shore and alongshore velocity spectra measured by the BASS sensor, and $\overline{f}$ is the mean frequency, defined by

$$\overline{f} = \frac{\int_0^{+\infty} fS(f)df}{\int_0^{+\infty} S(f)df}. \quad (2)$$

Similarly, the ratio of velocity variance along the minor principal axis to variance along the major axis was small (approximately 0.1) during both parts of the measurement period.

3. Analysis

3.1. Data Quality and Consistency

The BASS and the pressure sensor were operational during the entire measurement period. To assess the quality and consistency of the BASS and pressure records, it is instructive to compare the sum of cross-shore and alongshore velocity spectra determined from BASS measurements (denoted $S(f)$ in (1) and (2), where f is frequency) with the same quantity estimated from pressure measurements by means of linear wave theory [e.g., *Dean and Dalrymple* 1984]. Spectra computed in this manner consistently indicate excellent agreement near the spectral peak (see, for example, Figure 4), which is expected because the BASS was intentionally positioned sufficiently far from the bottom to be well outside of the wave boundary layer (Figure 1) and because previous measurements outside of the wave boundary layer indicate that the local relationship between pressure and velocity spectra is approximately consistent with linear wave theory [*Guza and Thornton*, 1980]. The spectral density determined from the BASS record is consistently much larger than the corresponding spectral density determined from the pressure record at high frequencies (Figure 4). The velocity spectrum at high frequencies is approximately proportional to $f^{-5/3}$, which indicates that the velocity variance at these frequencies is dominated by turbulence [e.g., *Monin and Yaglom*, 1971]. The spectra in Figure 4 indicate that the BASS and the pressure sensor functioned correctly and that the near-bottom velocity variance during the deployment period was dominated by surface gravity waves in the incident band at frequencies between roughly 0.05 and 0.5 Hz. These results are typical of both the first and second parts of the deployment period.

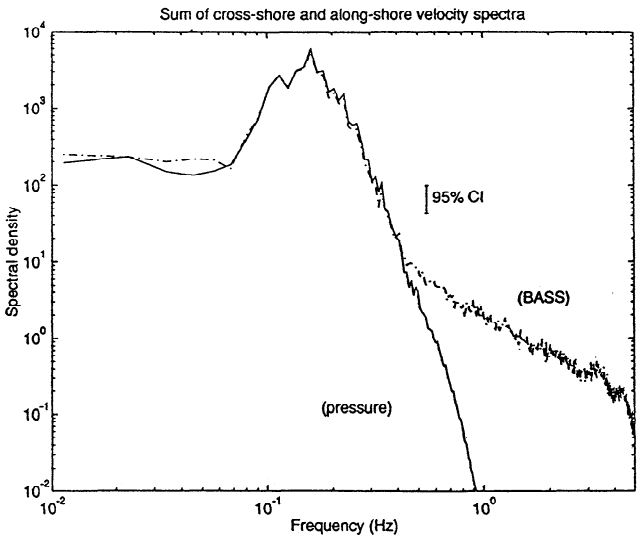

Figure 4. Velocity spectra estimated from 24 90-s BASS records and 24 concurrent 90-s pressure records beginning at approximately 2100 hours on December 5, 1992. The pressure spectrum has been converted to a velocity spectrum by means of linear wave theory. Units of spectral density are cm^{-2} s^{-2} Hz^{-1}. The pressure and BASS spectra agree well except at frequencies above approximately 0.4 Hz, where turbulence likely dominated the velocity variance, as explained in the text.

The alongshore LDV axis was operational during the entire deployment, and it produced valid data (as identified by the internal LDV processing) at a rate that varied from zero to slightly more than 80% of the nominal 25-Hz sample rate, when averaged over individual 90-s records. Because of the irregular and often relatively small effective sample rate, computation of spectra from LDV records was not instructive. The best way to evaluate the quality of the alongshore LDV measurements is to compare these measurements at the highest LDV position, which was intentionally sufficiently far from the bottom to be well outside of the wave boundary layer, with concurrent BASS measurements. This comparison indicates that measurements obtained by the two sensors are well correlated and approximately equal, with slightly different means and substantial scatter about a line with unit slope (Figure 5). BASS and LDV measurements compared in this way are not expected to be identical because the two sensors were at slightly

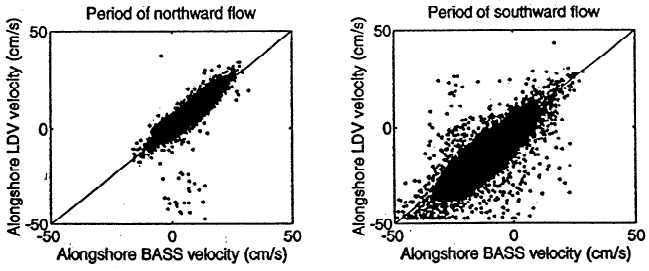

Figure 5. Instantaneous alongshore LDV velocity at the highest LDV measurement position versus concurrent alongshore BASS velocity during (left) the first part (1430 hours to 2200 hours on December 4) and (right) the second part (1400 hours on December 5 to 1000 hours on December 6) of the measurement period. The lines indicate equality between the LDV and BASS measurements. In Figure 5 (left) the few points outside of the central "cloud" of measurements occurred during three (of 20) 18–min data blocks, when the internal LDV processing was apparently set incorrectly, as explained in section 3.2. In Figure 5 (right) the absolute value of the velocity measured by the LDV could not exceed a threshold, set by the instrument, of approximately 48 cm s^{-1}. Although this threshold clearly influenced the measurements, it was sufficiently high so that it probably had a small effect on the analysis. The standard deviations of the difference between LDV and BASS measurements in the first and second parts of the measurement period are roughly consistent with statistically identical but completely uncorrelated turbulent velocity fluctuations at the two sensors, as explained in section 3.1.

different heights above bottom (roughly 16 cm for the topmost LDV measurement and approximately 20 cm for the BASS measurement) as well as being separated horizontally by a distance of approximately 70 cm (Figure 1). However, the agreement in Figure 5 between BASS and LDV measurements is consistent with the fact that the velocity variance was dominated by surface gravity waves, which vary vertically and horizontally over scales much longer than the separation between the two sensors.

Much of the difference between LDV and BASS measurements in Figure 5 can tentatively be attributed to turbulence produced by the alongshore current. To justify this statement, assume for the moment that velocity differences between the two measurements are solely a result of turbulence and that turbulent velocity fluctuations at the two sensors were statistically identical but completely uncorrelated. The variance σ_d^2 of the difference between alongshore velocities is then easily shown to be $2(v')^2$, where v' is the standard deviation of the alongshore turbulent velocity fluctuations. Existing measurements in turbulent channel flow [e.g., *Nezu and Rodi*, 1986] show that near the bottom $v' \simeq 2u_{*c}$, where u_{*c} is the shear velocity associated with the alongshore current. On the basis of this model, we expect that $\sigma_d \simeq 2^{3/2}\, u_{*c}$. In Figure 5 the standard deviation σ_d of the difference between BASS and LDV measurements was approximately 2.5 and 6.5 cm s^{-1} during the first and second parts of the deployment period, respectively. We estimate below (section 4) that u_{*c} was roughly 1 cm/s during the first part of the deployment and 2 cm/s during the second part. Thus σ_d was close to $2^{3/2}\, u_{*c}$ during both parts of the deployment.

The often small rate at which the alongshore LDV axis produced valid data might degrade estimates of low–order statistics (e.g., means and standard deviations) based on individual 90–s records. To assess this effect, we compare standard deviations and means based on 90–s records obtained by the alongshore LDV axis, at its highest measurement position, with corresponding statistics based on concurrent 90–s BASS records sampled at 10 Hz (Figure 6). The ratio of the standard deviation computed from the LDV record to the standard deviation computed from the BASS record asymptotes to unity, as expected, as the rate at which the LDV produced valid data increases (Figure 6, top). Similarly, the difference between the mean velocity computed from the LDV record and the mean velocity computed from the BASS record asymptotes to an approximately constant, near–zero value as the LDV data rate increases (Figure 6, bottom). The results in Figure 6 indicate that 90–s LDV records have sufficient measurements for meaningful computation of low–order statistics if the rate at which the LDV produced valid data is larger than roughly 8%.

The cross–shore axis of the LDV was problematic. In contrast to the wavelike records produced by the other sensors, this LDV axis produced noisy records, with

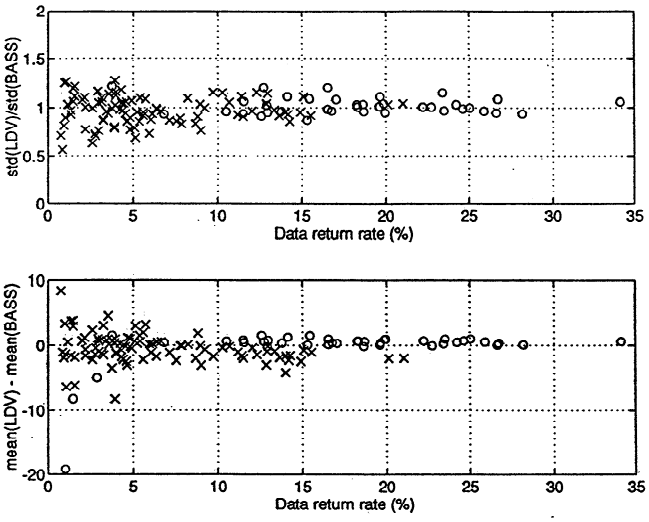

Figure 6. Comparison of statistics based on concurrent 90–s records obtained by the BASS and by the LDV, at its highest position, as a function of the rate at which the LDV returned valid measurements, including (top) ratio of standard deviations and (bottom) difference between the means for individual 90–s records. The circles and pluses indicate the first part (1430 hours to 2200 hours on December 4) and the second part (1400 hours on December 5 to 1000 hours on December 6) of the data set, respectively.

very little wavelike character during most of the deployment (Figure 7, top), apparently as a result of a flaw in the fiber–optic cable. During a brief period between 1813 and 2000 hours on December 4, 1992, however, the cross–shore LDV axis produced wavelike records within what appears to be noise (Figure 7, bottom). To extract the meaningful signal from these few records, we selected data points within ± 1 cm s^{-1} of a polynomial fit through the wavelike portion of the data [*Fredericks et al.*, 1994]. This procedure resulted in data at a rate between 25% and 50% of the nominal sample rate of 25 Hz, which is sufficiently large for meaningful computation of low–order statistics based on individual 90–s records, as shown in Figure 6.

LDV measurements of cross–shore velocity obtained at the highest measurement station by means of the above procedure are highly correlated with the concurrent BASS measurements of cross–shore velocity [*Fredericks et al.*, 1994]. For reasons that are not clear, however, the ratio between cross–shore LDV measurements at the highest station and concurrent cross–shore BASS measurements differs from the expected value of unity by a factor of approximately 3. To make the cross–shore LDV measurements consistent in amplitude with the concurrent cross–shore BASS measurements, we multiplied the cross–shore LDV velocities by a proportionality factor determined from the measurements at the highest LDV measurement station. Note that this procedure was not necessary for the alongshore LDV measurements (Figure 5).

The vertical position of the LDV was also somewhat problematic. The operator–controlled bottom–find procedure produced estimates of bottom elevation that were roughly consistent, as expected, with measurements of bottom position relative to fixed positions on the tripod that were obtained by scuba divers during the deployment and recovery [*Fredericks et al.*, 1994]. In addition, repeated tests before deployment and after recovery indicated that the LDV profiling mechanism correctly moved the LDV through its array of sampling positions at 0.5, 1.0, 2.0, 4.0, 8.0, and 16.0 cm above a nominal bottom. However, two commands to return the LDV to its highest possible ("home") position, which were issued between sampling periods during the course of the experiment, resulted in an unexpected number of steps by the stepper motor that moved the profiler, indicating that the LDV profiler was not at the position that we expected when we issued the commands. These results indicate that the elevations of the LDV measurement positions, relative to each other, were consistent with our plans, but the absolute elevations of the LDV measurement stations, relative to the bottom or to other instruments on the tripod, were not known with certainty. The estimated uncertainty of the absolute LDV elevations is a few centimeters, which is sufficiently large to be a potential problem, since this uncertainty is comparable to the estimated thickness of the wave boundary layer (see section 4).

The video camera functioned during the entire deployment. As noted in section 2.2, however, it did not produce usable images of the bottom during the second part of the deployment period, when there was substantial suspended material in the water column.

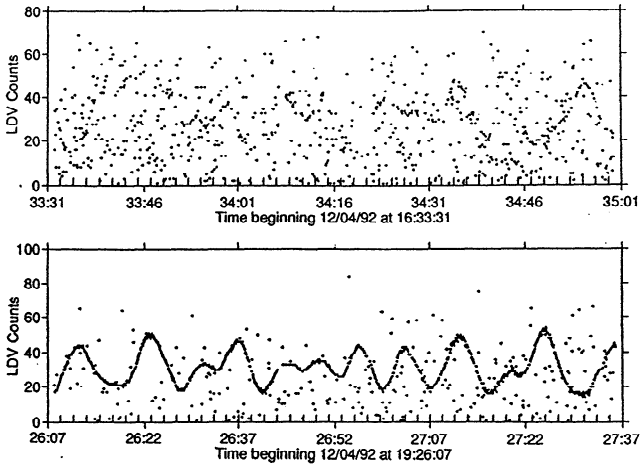

Figure 7. Examples of 90–s records obtained from the cross–shore LDV axis at the highest measurement position in which (top) no wavelike character is evident and (bottom) a wavelike signal is evident within noise. LDV counts on the vertical axes are proportional to velocity.

3.2. Periods Selected for Analysis

Because of uncertainties in the absolute elevation of the LDV measurement stations (section 3.1), our analysis focuses on two periods during which the LDV measurements themselves clearly indicate the presence of the bottom. During both periods, the forcing was approximately stationary, so that the individual 90–s records obtained during each period may reasonably be regarded as independent realizations of the same process. In addition, the elevation of the nominal bottom, to which the LDV measurement stations were referenced, was fixed during both periods, so that the positions of the LDV measurement stations, relative to the tripod, did not change.

The first period, termed glimpse 1, was the entire first part of the deployment, between approximately 1430 and 2200 hours on December 4, during which the mean alongshore flow was northward (Figure 3). During glimpse 1 there were 20 18–min data blocks. Of these we omit from the analysis three blocks, between 1708 and 1808 hours, during which there was apparently an operator error in setting the internal LDV criteria for identifying valid measurements. These three blocks account for all of the anomalous points outside of the central "cloud" of measurements in Figure 5 (left), and the standard deviations of LDV velocity in these blocks were many times the corresponding standard deviations in neighboring blocks. Thus the analysis of glimpse 1 is based on 17 data blocks, each containing two 90–s records at each LDV measurement position, so that there is a total of 34 90–s alongshore LDV records at each station, each with a concurrent BASS record.

Glimpse 1 includes the period during which the cross–shore LDV axis produced usable results. There were five

18–min data blocks in which the cross–shore LDV axis produced usable measurements. Each block contains two 90–s records at each LDV measurement station, so that there is a total of 10 90–s cross–shore LDV records at each station, each with a concurrent BASS record.

The second period selected for analysis, termed glimpse 2, was between 1744 and 2014 hours on December 5, during the second part of the deployment period, when the mean alongshore flow was southward (Figure 3). During glimpse 2 there were seven 18–min data blocks, each containing two 90–s records at each LDV measurement station, so that there was a total of 14 90–s alongshore LDV records at each position, each with a concurrent BASS record.

Histograms of LDV measurements at all six measurement stations are a convenient way to demonstrate how the LDV measurements indicate the presence of the bottom. During glimpse 1 (Figure 8) the measurements at the highest three positions yielded a moderate data return (10% to 20%) and nonzero velocities, indicating that the LDV sensing volume was always in the water column at these heights. The histogram at the fourth–highest position is similar but indicates an anomalous peak at zero velocity, suggesting coincidence with the bottom during a small part of the measurement period. In contrast, the record at the fifth–highest position yields a substantially larger data return at a velocity of almost precisely zero, indicating close proximity of the LDV sensing volume to the bottom. The record at the lowest position indicates a smaller data return at essentially zero velocity, suggesting that the LDV sensing volume was at or below the bottom during most of the record. These histograms indicate clearly that only the top four LDV measurement stations should be included in the analysis of glimpse 1 and that the effective bottom was probably between the fourth–highest and fifth–highest measurement stations. Similar results occur during glimpse 2 (Figure 9). The histograms in Figure 9 indicate that only the top three measurement stations should be included in the analysis of glimpse 2 and that the effective bottom during glimpse 2 was between the third–highest and fourth–highest measurement positions.

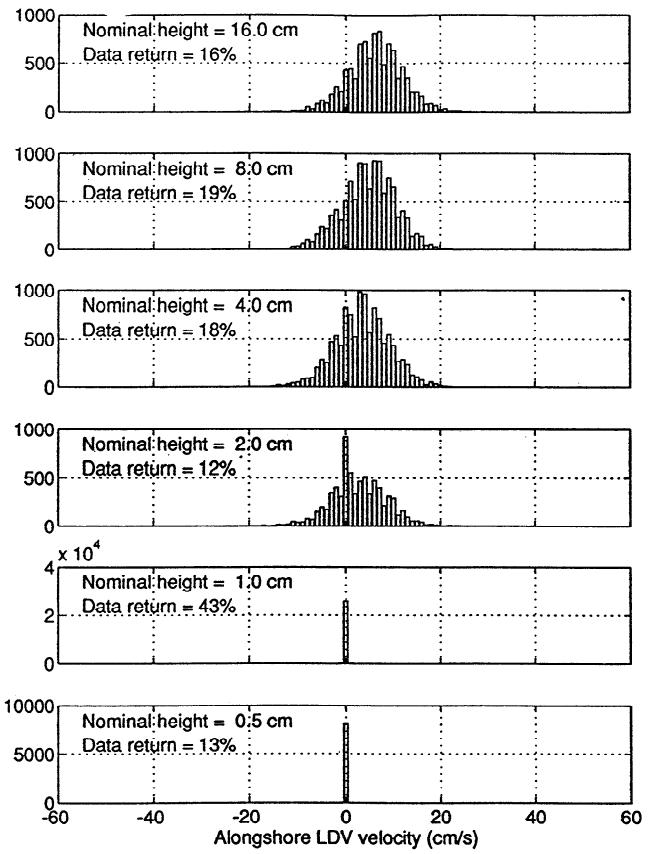

Figure 8. Histogram of alongshore LDV velocity measurements during glimpse 1. The nominal heights are the heights above the nominal bottom used to define LDV sampling positions. Note that the rate at which the LDV obtained valid data varies between 10% and 20% at the top four measurement positions and that there clearly were velocity fluctuations at these heights. In contrast, the data return rate at the second–lowest position is much larger and nearly all of the measurements show zero velocity, indicating close proximity to the bottom. Note the change in vertical scale in the bottom two histograms.

In all but ten of 136 90–s LDV records at the highest four measurement stations in glimpse 1 and in all but two of 56 90–s records at the highest three measurement stations in glimpse 2, the LDV returned valid measurements of alongshore velocity at a rate greater than 8% of the nominal 25–Hz sample rate. Thus, according to the results in Figure 6, almost all of the individual 90–s records selected for analysis in glimpses 1 and 2 had LDV data sufficient for computation of meaningful low–order statistics.

3.3. Quantitative Characterization of the Measurements

To examine the irregularly and sparsely sampled LDV measurements for the features expected in a wave boundary layer, we define the dimensionless amplitude a to be the ratio of the standard deviation of a given LDV record to the standard deviation of the concurrent BASS record, and we define the corresponding phase ϕ of the LDV with respect to the BASS to be $2\pi\overline{f}\tau$, where $\overline{f}$ is the mean frequency based on the sum of cross–shore and alongshore velocity spectra obtained from BASS measurements, defined by (2), and τ is the lag at which the maximum correlation between BASS and LDV measurements occurred in the given record. The phase ϕ is defined to be positive if the LDV velocity leads the BASS velocity. The quantities a and ϕ are defined separately for the alongshore and cross–shore components of the velocity.

For each of glimpses 1 and 2 we computed the dimensionless amplitude a and phase ϕ for the alongshore velocity and separately for the cross–shore velocity (when the cross–shore LDV axis produced usable results) based on measurements in each 90–s record. We then used this ensemble to compute means and 95% confidence intervals, assuming Gaussian statistics, for a

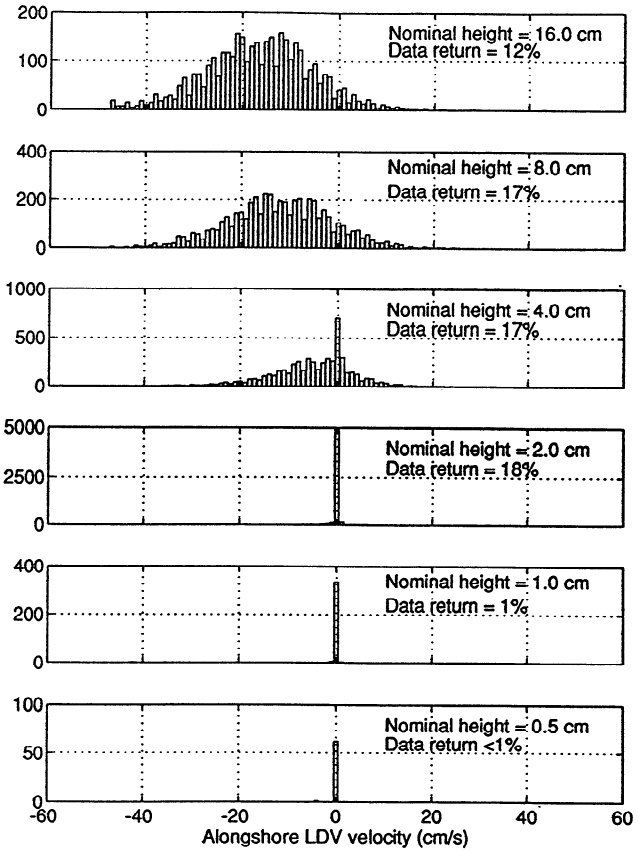

Figure 9. Histogram of alongshore velocity measurements during glimpse 2. The nominal heights are the heights above the nominal bottom used to define LDV sampling positions. The rate at which the LDV returned valid data varied between 10% and 20% at the top three measurement positions, and there clearly were nonzero velocity fluctuations at these heights. In contrast, almost all of the measurements at the fourth-highest measurment station indicate zero velocity, suggesting close proximity to the bottom. Note the changes in vertical scale, particularly in the fourth-highest histogram.

and ϕ as functions of height z above bottom during each glimpse. We used the same method to compute means and 95% confidence intervals for the mean alongshore velocity and cross-shore velocity (when the cross-shore axis of the LDV produced usable results). We corrected the phase estimates for the horizontal spatial displacement of the BASS and LDV sensors based on estimates (Figure 3) of the dominant frequency and direction of the waves.

We have not attempted quantative analyses of the video images. The video images are sufficient to show, however, that the bottom during glimpse 1 was rippled, with short crests and a ripple wave length of roughly 10 cm, as noted in section 2.2. The video images during glimpse 1 also showed that the LDV did not occupy a fixed position with respect to a single ripple during glimpse 1. Instead, ripples migrated slowly beneath the LDV during the course of glimpse 1, so that the measurements during glimpse 1 represent a horizontal spatial average over several ripples. Because of the variability of the estimates of amplitudes and phase during individual 90-s records, we have not attempted to isolate periods during glimpse 1 when the LDV occupied a specific position with respect to a particular ripple. As noted in section 2.2, the video images gave no information about the bottom during glimpse 2.

3.4. The Grant–Madsen Model

The eddy viscosity model proposed by *Grant and Madsen* [1979] (hereinafter referred to as the Grant-Madsen model) provides a useful vehicle for analysis of the present measurements. This model addresses the case of a steady current interacting with monochromatic, unidirectional waves over a rough bottom, with roughness elements small in comparison to the thickness of the wave boundary layer. Although more recent models have been developed (see, for example, the review by *Sleath* [1990]) and some of the newer models have shown to produce results in slightly better agreement with existing laboratory measurements than the Grant–Madsen model [e.g., *Brevik*, 1981], the differences between calculations based on the different models are small, and use of the Grant–Madsen model is convenient because of its simplicity. The weak-current approximation to the model, in which the wave-induced oscillatory bottom stress is large in comparison to the stress produced by the steady current, is appropriate under conditions of interest here (see section 4).

To apply the Grant–Madsen model, it is convenient to define the x and y axes to be oriented in the cross-shore and alongshore directions, respectively, and to define the z axis to be vertical, with $z = 0$ at the bottom and z positive upward. It is also convenient to let the direction of wave propagation be parallel to the x_1 axis, which is inclined at an angle θ to the x axis, where θ is the angle of incidence. The velocity components in the x and y directions are u and v, respectively, and the wave-induced velocity in the x_1 direction is denoted u_1. For simplicity it is convenient to assume that the mean flow is solely in the y direction, which is approximately but not precisely consistent with the observations (Figure 3).

The model representation of the wave-induced oscillatory velocity is $u_1(z,t) = \mathrm{Re}[\hat{u}(z)\exp(i\omega t)]$, where t is time, Re denotes the real part of a complex expression, $\hat{u}(z)$ is a complex function, and ω is the radian frequency of the waves. The model solution for the oscillatory velocity is

$$\hat{u}(z) = \hat{u}_\infty \left[1 - \frac{\ker\left(2\sqrt{\zeta}\right) + i\,\mathrm{kei}\left(2\sqrt{\zeta}\right)}{\ker\left(2\sqrt{\zeta_0}\right) + i\,\mathrm{kei}\left(2\sqrt{\zeta_0}\right)}\right], \quad (3)$$

where $\hat{u}_\infty$ is the free-stream complex velocity just outside of the wave boundary layer, ζ is $(z - \Delta)/\ell$, ζ_0 is z_0/ℓ, and ker and kei are zeroth-order Kelvin functions [e.g. *Abramowitz and Stegun*, 1970]. The quantity Δ is the displacement height of the bottom [e.g., *Monin and Yaglom*, 1971; *Jackson*, 1981], which defines the

effective location of the bottom with respect to the position $z = 0$, which has an ambiguous definition when the bottom is rough. The quantity z_0 is the bottom roughness parameter and ℓ is a scale height equal to $\kappa u_{*cw}/\omega$, where κ is von Karman's empirical constant (approximately equal to 0.40), ω is the radian frequency, and u_{*cw} is the shear velocity characteristic of the wave boundary layer. In the weak–current approximation, u_{*cw} is determined by

$$u_{*cw} = \frac{\kappa}{2} \frac{| \hat{u}_\infty |}{N_0(2\sqrt{\zeta_0})}, \tag{4}$$

where $N_0 = (\mathrm{ker}^2 + \mathrm{kei}^2)^{1/2}$. Equations (3) and (4) determine ℓ, u_{*cw}, and $\hat{u}(z)$ for given ω, $\hat{u}_\infty$, z_0, and Δ.

On the basis of the above solution for the wave–induced velocity, the model representation of the dimensionless amplitude a and phase ϕ, defined in section 3.3, is

$$a \exp(i\phi) = 1 - \frac{\mathrm{ker}\,(2\sqrt{\zeta}) + i\,\mathrm{kei}\,(2\sqrt{\zeta})}{\mathrm{ker}\,(2\sqrt{\zeta_0}) + i\,\mathrm{kei}\,(2\sqrt{\zeta_0})}. \tag{5}$$

Note that this expression describes the dimensionless amplitude and phase of the wave–induced velocity in the x_1 direction, and it also describes the dimensionless amplitude and phase of the projection of the wave–induced velocity in the x and y directions.

The model representation of the steady alongshore current is $\overline{v}(z)$. The model solution for the steady velocity is

$$\overline{v}(z) = \frac{u_{*c}^2}{\kappa u_{*cw}} \log\left(\frac{z - \Delta}{z_0}\right) \tag{6}$$

for $z - \Delta < \delta_{cw}$ and

$$\overline{v}(z) = \frac{u_{*c}^2}{\kappa u_{*cw}} \log\left(\frac{\delta_{cw}}{z_0}\right) + \frac{u_{*c}}{\kappa} \log\left(\frac{z - \Delta}{\delta_{cw}}\right) \tag{7}$$

for $z - \Delta > \delta_{cw}$. Here δ_{cw} is the thickness of the wave boundary layer and u_{*c} is the shear velocity based on the mean bottom stress. *Grant and Madsen* [1979] proposed that $\delta_{cw} = 2\ell$. Equations (6) and (7) determine $\overline{v}(z)$ for given u_{*c}, u_{*cw}, z_0, and Δ.

Application of the Grant–Madsen model to our measurements can be undertaken in a number of slightly different ways. Here we estimate ω as $2\pi\overline{f}$, where $\overline{f}$ is the mean frequency based on BASS measurements, defined by (2). We define the x_1 direction to be the principal direction based on the BASS velocity measurements, and we determine $| \hat{u}_\infty |$ by requiring the model representation of the velocity variance outside of the wave boundary layer, which is $(1/2) | \hat{u}_\infty |^2$, to equal the variance in the x_1 direction determined by the BASS measurements. We estimate the roughness parameter z_0 and the displacement height Δ by means of a model fit to the LDV estimates of dimensionless amplitude a and phase ϕ averaged over each glimpse. The model fit is based on an iterative least squares procedure that minimizes the sum of the squared absolute values of the differences between model values and measurements of $a \exp(i\phi)$. We obtain crude estimates of 95% confidence intervals for $\log_{10}(z_0)$ and Δ by linearizing the nonlinear least squares problem about the best fit values [e.g., *Draper and Smith*, 1966] and assuming Gaussian underlying statistics. Finally, we estimate u_{*c}, the shear velocity associated with the mean alongshore bottom stress, by fitting the model expression (7) to LDV measurements of $\overline{v}$ outside of the wave boundary layer for each 90–s record. We use this ensemble to estimate means and 95% confidence intervals, assuming Gaussian underlying statistics, for u_{*c} during each of glimpses 1 and 2.

4. Results

4.1. Glimpse 1

During glimpse 1 the mean alongshore flow was poleward, surface waves were incident from the east–southeast, and the bottom was rippled with a ripple wavelength of roughly 10 cm, as described in section 2.2. The values of free–stream velocity $| \hat{u}_\infty |$ and radian frequency ω, determined as described in section 3.4, were 15.8 cm s^{-1} and 0.69 s^{-1}, respectively. In the following, $z = 0$ coincides with the nominal bottom used in defining the elevations of the LDV measurements (see Figure 8).

Estimates of dimensionless amplitude a and phase ϕ based on measurements of cross–shore velocity during glimpse 1 are consistent with qualitative expectations as well as being consistent with calculations based on the fit to the Grant–Madsen model (Figure 10, top). The dimensionless amplitude and the phase approach unity and zero, respectively, outside of the wave boundary layer, and the amplitude decreases while the phase increases with increasing proximity to the bottom. The values of Δ and $\log_{10}(z_0)$ (in cgs units), determined from the model fit as described in section 3.4, are 1.46 ± 0.51 and -1.36 ± 0.69, respectively, so that the best fit value of z_0 is approximately 0.044 cm. The best fit value of Δ is consistent with the idea (based on histograms in Figure 8) that the effective bottom was located between the second–lowest and third–lowest LDV measurements. The values of boundary layer thickness δ_{cw} and wave–induced shear velocity u_{*cw} based on the best fit values of the model parameters are 2.68 and 2.31 cm s^{-1}, respectively. The model fit is controlled by the lowest measurement of dimensionless amplitude and the lowest two measurements of phase, which are the only measurements that indicate clearly the presence of the wave boundary layer (Figure 10, top).

In contrast to the Grant–Madsen model, which predicts that the vertical structure of dimensionless amplitude a and phase ϕ are the same for both the alongshore and cross–shore components of the wave–induced velocity, the measurements indicate qualitatively that the vertical structure of the alongshore flow differs from that of the cross–shore flow (Figure 10, bottom). Estimates of a based on alongshore velocity indicate no wave boundary layer, or perhaps, a slight increase in amplitude associated with the outer edge of a thin boundary

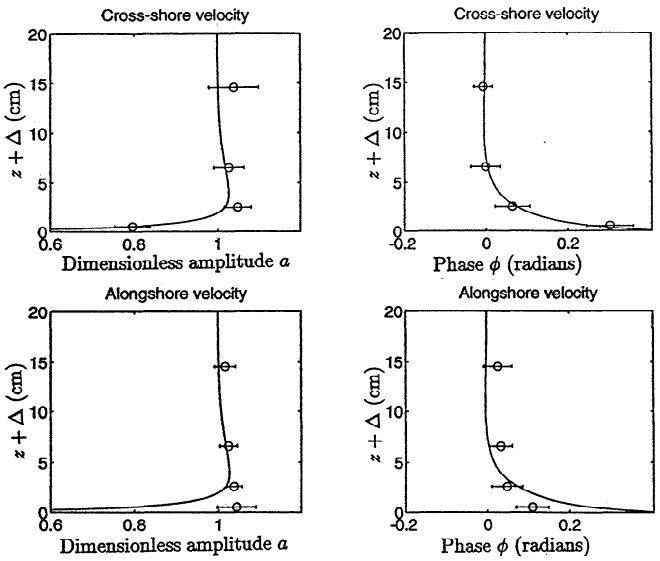

Figure 10. Vertical structure of wave-induced velocities during glimpse 1, showing (top left) dimensionless amplitude a and (top right) phase ϕ for the cross-shore flow, and (bottom left) dimensionless amplitude a and (bottom right) phase ϕ for the alongshore flow. In all cases the circles are based on the measurements and the corresponding error bars represent 95% confidence intervals, obtained as explained in the text. The solid line represents the model fit of the *Grant and Madsen* [1979] model (Grant-Madsen model) to the measurements of amplitude and phase for the cross-shore flow. The values of the bottom-related parameters used in the model calculations are $z_0 = 0.044$ cm and $\Delta = 1.46$ cm.

layer (Figure 10, bottom left). Estimates of ϕ based on alongshore velocity are smaller than estimates of ϕ based on cross-shore velocity (Figure 10, bottom right), again indicating a thinner boundary layer than is associated with the cross-shore flow. The indication of a thinner wave boundary layer suggests that the bottom roughness experienced by the alongshore flow was smaller than that experienced by the cross-shore flow.

Although the measurements in Figure 10 suggest qualitatively that the bottom roughness experienced by the alongshore flow was smaller than that experienced by the cross-shore flow, quantitative results based on a fit to the Grant–Madsen model indicate that the measurements are not sufficient to reject a simpler interpretation in which both components of the flow experience the same bottom roughness. The best fit model estimates of Δ and $\log_{10}(z_0)$ (in cgs units) based on the alongshore measurements of a and ϕ are -10.26 ± 13.42 and 0.06 ± 1.41, respectively. The model fit places the measured values of a and ϕ at the extreme outer edge of a relatively thick wave boundary layer, with a bottom roughness that is actually larger, although not significantly different, than indicated by the cross-shore flow. The best fit model estimates must be regarded as nonsensical because they place the effective bottom far below the bottom indicated by the histograms in Figure 8. If Δ is constrained to be 1 cm, which is the smallest value consistent with Figure 8, then the best fit model estimate of $\log_{10}(z_0)$ is -2.13 ± 1.20, which is smaller, but again, not significantly different from the bottom roughness indicated by the cross-shore flow. Because of these results, the values of z_0 and Δ used in the model calculations in Figure 10 (top and bottom) are based on the model fit to the cross-shore measurements (i.e., $\Delta = 1.46$ cm and $z_0 = 0.044$ cm).

Measurements during glimpse 1 indicate an extremely weak mean cross-shore velocity (Figure 11, top). The uncertainties of tripod and isobath orientation are sufficiently large that the measurements of mean cross-shore flow are not meaningful.

Measurements of mean alongshore velocity during glimpse 1 are meaningful, however. The presentation of these measurements is based on $\Delta = 1.46$ cm, as determined in the model fit to estimates of a and ϕ based on the cross-shore velocity measurements. The measurements of mean alongshore velocity clearly indicate a departure within the wave boundary layer from the logarithmic structure that occurs outside of the wave boundary layer (Figure 11, bottom). This feature, which is the primary result of the Grant–Madsen model, persists qualitatively in the measurements even if the

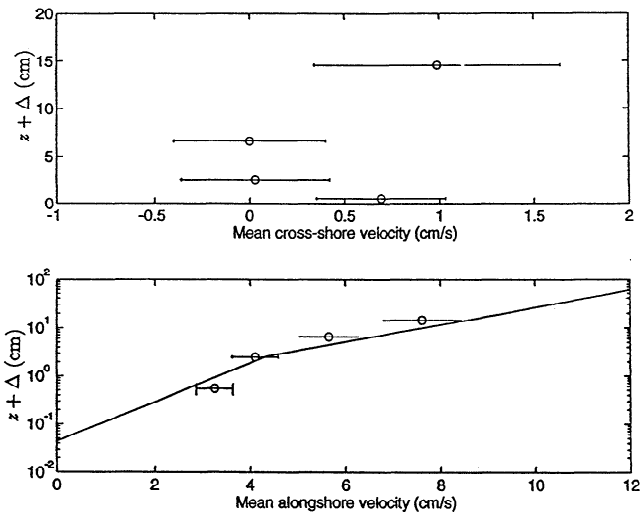

Figure 11. Vertical structure of (top) the mean cross-shore velocity and (bottom) the mean alongshore velocity during glimpse 1. The circles are based on the measurements, and the corresponding error bars represent 95% confidence intervals, obtained as explained in the text. Here $\Delta = 1.46$ cm, as determined in the fit of the Grant–Madsen model to the estimates of amplitude and phase based on the cross-shore velocity measurements shown in Figure 10. The solid line in Figure 11 (bottom) represents calculations based on the Grant–Madsen model with $z_0 = 0.044$ cm, $\Delta = 1.46$ cm, $\omega = 0.69$ s^{-1}, $u_{*c} = 0.99$ cm s^{-1}, and $u_{*cw} = 2.31$ cm s^{-1}. The values of z_0, Δ, and u_{*cw} were determined from the model fit to the measurements of amplitude and phase of the cross-shore velocity shown in Figure 10. The estimate of u_{*c} is based on a model fit to the top two measurements of alongshore velocity.

estimated uncertainty in Δ (± 0.51 cm) is taken into account. To see this, note that only the bottommost data point on the semilogarithmic plot of alongshore velocity (Figure 11, bottom) is significantly affected by the uncertainty in Δ. The most extreme modification associated with the uncertainty in Δ would be to move this point from $z + \Delta \simeq 0.5$ cm to $z + \Delta \simeq 1.0$ cm, which reduces but still retains the curvature in the plot, indicating a departure from a purely logarithmic mean velocity profile.

Model computations of $\overline{v}(z)$ require an estimate of u_{*c}, the shear velocity associated with the mean bottom stress, based on (7). With $\Delta = 1.46$ cm, $z - \Delta$ is larger than δ_{cw} only at the top two LDV measurement stations. A fit of (7) to these measurements indicates that $u_{*c} = 0.99 \pm 0.16$ cm s^{-1}. Thus the mean bottom stress is approximately 5 times smaller than the maximum wave–induced bottom stress, which is sufficiently small that the weak–current approximation to the Grant–Madsen model is justified. Model calculations of mean alongshore velocity based on $\Delta = 1.46$ cm, $z_0 = 0.044$ cm, $u_{*cw} = 2.31$ cm s^{-1}, $\delta_{cw} = 2.68$ cm, and $u_{*c} = 0.99$ cm s^{-1} are quite consistent with measurements (Figure 11, bottom). Note that outside the wave boundary layer, the model calculation of $\overline{v}$ is constrained to coincide in slope (on a semilogarithmic plot) with the measurements because the estimate of u_{*c} is based on these measurements. The intercept is not constrained to coincide with the top two measurements in this manner, however.

4.2. Glimpse 2

During glimpse 2 the mean alongshore flow was equatorward and surface waves were incident from the east–northeast (Figure 3). The values of free–stream velocity $|\hat{u}_\infty|$ and radian frequency ω, determined as described in section 3.4, were 35.51 cm s^{-1} and 1.00 s^{-1}, respectively. In the following, as in section 4.1, $z = 0$ coincides with nominal bottom used in defining the locations of the LDV measurements (see Figure 9).

As in glimpse 1, estimates of dimensionless amplitude a and phase ϕ based on alongshore velocity measurements during glimpse 2 indicate the qualitative features that are expected in a wave boundary layer, and they are also consistent with the fit to the Grant–Madsen model (Figure 12, top). The model–fit estimates of Δ and $\log_{10}(z_0)$ (in cgs units) are 3.61 ± 0.97 and -1.54 ± 0.85, respectively, so that the best fit value of z_0 is 0.029 cm. The best fit value of Δ is consistent with the idea (based on histograms in Figure 9) that the effective bottom was located between the third–lowest and fourth–lowest LDV measurement positions. The values of boundary layer thickness δ_{cw} and wave–induced shear velocity u_{*cw} based on the best fit values of the model parameters are 3.44 cm and 4.29 cm s^{-1}, respectively. The model fit is controlled primarily by the lowest amplitude and phase measurements, which are the only measurements that indicate clearly the presence of the wave boundary layer (Figure 12, top).

As in glimpse 1, measurements of mean alongshore velocity during glimpse 2 indicate a departure within

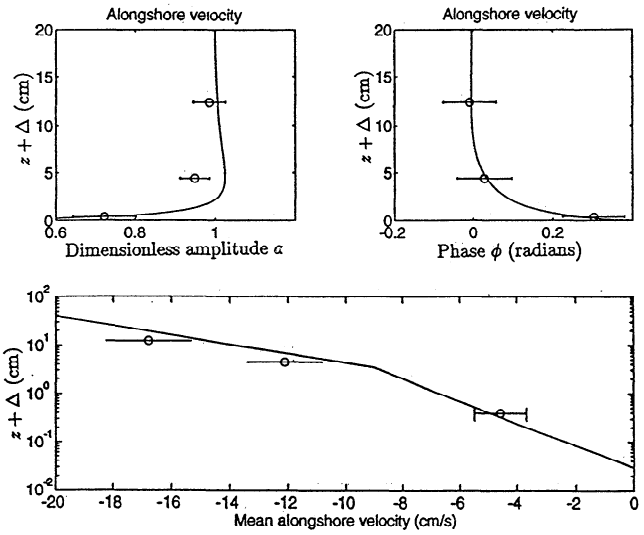

Figure 12. Vertical structure of alongshore velocity during glimpse 2, showing (top left) dimensionless amplitude a, (top right) phase ϕ, and (bottom) mean alongshore velocity. The circles are based on the measurements, and the error bars represent 95% confidence intervals, computed as explained in the text. Here $\Delta = 3.61$ cm, as obtained in the fit of the Grant–Madsen model to the amplitude and phase measurements. The solid lines represent calculations based on the Grant–Madsen model, with $\Delta = 3.61$ cm, $z_0 = 0.029$ cm, $u_{*cw} = 4.29$ cm s^{-1}, $u_{*c} = 1.80$ cm s^{-1}, and $\omega = 1.00$ s^{-1}. The values of z_0, Δ, and u_{*cw} are based on the model fit to the amplitude and phase measurements. The value of u_{*c} is based on a model fit to the top two measurements of alongshore velocity.

the wave boundary layer from the purely logarithmic behavior outside the wave boundary layer (Figure 12, bottom) provided that $\Delta = 3.61$ cm, as determined in the model fit to the measurements of amplitude and phase. In glimpse 2, however, the uncertainty in Δ (estimated as ± 0.97 cm) is large enough so that a conventional, purely logarithmic mean velocity profile could not be rejected on the basis of the measurements. To see this, note that the uncertainty in Δ significantly influences only the bottom data point in the semilogarithmic plot of mean velocity (Figure 12, bottom). The maximum effect that the uncertainty in Δ could have would be to move this point from $z + \Delta \simeq 0.4$ cm to $z + \Delta \simeq 1.4$ cm. This modification would place the bottom data point almost precisely on a straight line through the other two data points, indicating a purely logarithmic mean velocity profile.

Model calculations of $\overline{v}$ require an estimate of u_{*c}. With $\Delta = 3.61$ cm and $\delta_{cw} = 3.44$ cm, $z - \Delta$ was larger than δ_{cw} only at the top two LDV measurement stations during glimpse 2, and a fit of (7) to measurements of $\overline{v}$ at these stations gives $u_{*c} = 1.80 \pm 0.41$. According to this estimate, the mean bottom stress was approximately 6 times smaller than the maximum wave–induced bottom stress, so that the weak–current approximation to the Grant–Madsen model is justified, as in glimpse 1.

Model calculations of mean alongshore velocity based on $\Delta = 3.61$ cm, $z_0 = 0.029$ cm, $u_{*cw} = 4.29$ cm s^{-1}, $\delta_{cw} = 3.44$ cm, and $u_{*c} = 1.80$ cm s^{-1} are quite consistent with the measurements (Figure 12, bottom).

5. Discussion

The approximate consistency between measurements and model calculations of dimensionless amplitude a and phase ϕ (Figures 10 and 12, top) supports the ability of the Grant–Madsen model to represent realistically the structure of the wave-induced flow in the wave boundary layer. The model physics are gradient transport of momentum by means of an eddy viscosity equal to $\kappa u_{*cw}(z - \Delta)$, where κ is von Karman's constant, u_{*cw} is the shear velocity associated with the maximum bottom stress, and $z - \Delta$ is height above the effective bottom, as before. Use of more recent models [e.g., *Brevik*, 1981] has a slight effect on calculations of amplitude and phase, including, in particular, a slight increase in "overshoot" (the amount by which the maximum amplitude within the boundary layer exceeds the free-stream amplitude). A small increase in overshoot slightly improves the agreement between model calculations and measurements of cross-shore flow in glimpse 1 (Figure 10, top) but slightly worsens it in glimpse 2 (Figure 12, top).

The agreement between measurements and model calculations of mean alongshore velocity (Figures 11 (bottom) and 12 (bottom)) supports the ability of the Grant–Madsen model to represent realistically the structure of the mean current in a wave boundary layer. In particular, the measurements indicate a departure within the wave boundary layer from a purely logarithmic mean velocity profile, which is one of the most important predictions of the Grant–Madsen model. Although the present measurements and analysis indicate this feature in both glimpses 1 and 2 (Figures 11 (bottom) and 12 (bottom)), it is important to recall that the uncertainty of bottom location in glimpse 2 is sufficiently large that a simpler model, with a purely logarithmic mean velocity profile, cannot be rejected on the basis of the measurements. The distortion of the mean velocity profile occurs in the Grant–Madsen model because of an enhanced eddy viscosity within the wave boundary layer, associated with turbulence intensities produced not only by the mean bottom stress, but also by the larger wave-induced bottom stress. The primary effect of using a more recently developed model (see, for example, the review by *Sleath* [1990]) would be to introduce a smooth transition in mean velocity gradient at the top of the wave boundary layer, as opposed to the abrupt change indicated by the Grant–Madsen model (Figures 11 (bottom) and 12 (bottom)). This refinement is not particularly important in the present application.

The distortion of the mean velocity profile within the wave boundary layer results in an "apparent" roughness, perceived by the mean flow outside of the wave boundary layer, which is larger than the "physical" bottom roughness parameter z_0 [*Grant and Madsen*, 1979]. During both of glimpses 1 and 2, the present measurements and analysis (Figures 11 (bottom) 12 (bottom)) indicate that the apparent roughness (~ 0.5 cm) was larger by an order of magnitude than the physical roughness (~ 0.05 cm). This increase in apparent roughness corresponds to an increase in bottom drag coefficient, for example, at a height of 100 cm above bottom, by a factor of approximately 2, which is potentially important in some applications.

The present estimates of the bottom roughness parameter z_0 are consistent with existing semiempirical representations of the characteristics of wave-formed sand ripples. During glimpse 1 the video images indicated a ripple wavelength λ of approximately 10 cm (section 2.2), which is consistent with occurrence of anorbital ripples [*Wiberg and Harris*, 1994] with a length of approximately $500d$, where d is the sand grain diameter. Video images did not provide information about the bottom during glimpse 2, but *Wiberg and Harris*'s [1994] expressions indicate that anorbital ripples with $\lambda \simeq 500d \simeq 10$ cm were present during that period, and video images of the bottom after glimpse 2 but before recovery of the tripod are consistent with this result (section 2.2). The existing semiempirical estimate of the hydrodynamic roughness of wave-formed sand ripples is $z_0 = \eta^2/\lambda$, where η is the ripple height. On the basis of this expression, the present best fit estimates of $z_0 \simeq 0.044$ cm and $z_0 \simeq 0.029$ cm during glimpses 1 and 2 correspond to $\eta \simeq 0.7$ cm and $\eta \simeq 0.5$ cm, respectively. These values are not precisely consistent with *Wiberg and Harris*'s [1994, Figure 7b] empirical expressions for ripple height, but they are within the experimental scatter around those expressions. Note that during both glimpses 1 and 2 the ratio of ripple height to boundary layer thickness was relatively small (although not negligible), as assumed in the Grant–Madsen model.

As noted in section 4.1, measurements of amplitude and phase for the alongshore flow in glimpse 1 (Figure 10, bottom) qualitatively suggest a thinner boundary layer, possibly corresponding to a smaller bottom roughness, than is associated with the cross-shore flow. A dependence of bottom roughness on flow direction is plausible because the roughly shore-parallel ripple crests might present more obstruction to the cross-shore flow than to the alongshore flow. This idea has been suggested on theoretical grounds [*Madsen*, 1991], and it has also been supported observationally by previous measurements outside of the wave boundary layer [*Drake et al.*, 1992]. As also noted in section 4.1, however, model-fit estimates of bottom roughness indicate that the amplitude and phase measurements during glimpse 1 are not sufficient to reject a simpler model in which the bottom roughness is identical for both the alongshore and cross-shore flows. Similarly, measurements of mean alongshore flow during glimpse 1 are insufficent to reject a model in which the bottom roughness experienced by the alongshore flow is identical to that experienced by the cross-shore flow (Figure 11, bottom). Lack of a significant dependence of bottom roughness on flow direction, in spite of the anisotropy

of wave–formed sand ripples, might occur because of the relatively short ripple crests (which produce a spatially complex bottom roughness field) and because the ripple crests were not precisely parallel to the coastline. On the other hand, lack of a significant dependence of bottom roughness on flow direction might occur in our results simply because the uncertainty of our bottom roughness estimates is relatively large.

An effect not included in our analyis is stratification by suspended sediments [e.g., *Monin and Yaglom*, 1971]. In the absence of sediment concentration measurements, model calculations provide useful estimates of the importance of this effect. In the model developed by *Glenn and Grant* [1987] the importance of sediment stratification is measured by $\beta(z-\Delta)/L$, where β is an empirical constant, $z-\Delta$ is height above the effective bottom, as before, and L is the Monin–Obukhov length. Calculations based on Glenn and Grant's model indicate that even a modest effect of sediment stratification $[\beta(z-\Delta)/L = 0.1]$ requires sediment concentrations far above the values indicated by the model itself and also well above measured values of near–bottom sediment concentration in other nearshore observational studies [*Hay and Sheng*, 1992]. Thus the information that exists at present justifies neglect of sediment stratification in the analysis of our measurements.

6. Summary and Conclusions

We have presented measurements obtained with a profiling laser–Doppler velocimeter in the wave boundary layer over a sand beach during two periods of approximately stationary forcing, each with a duration of several hours, termed glimpse 1 and glimpse 2. As expected in a wave boundary layer, the measurements indicate a reduction in amplitude and an increase in phase, relative to the overlying flow, with increasing proximity to the bottom. Measurements of mean alongshore velocity indicate the distortion of the mean current within the wave boundary layer that is one of the most important predictions of the eddy viscosity model developed by *Grant and Madsen* [1979], although the uncertainty of the bottom position was sufficiently large during glimpse 2 that a simpler model, with a purely logarithmic velocity profile, could not be rejected on the basis of the measurements. Measurements of amplitude and phase are approximately consistent with a fit to the Grant–Madsen model in which the roughness and effective elevation of the bottom are adjustable parameters. Model–fit estimates of bottom roughness are approximately consistent with existing semiempirical representations of the characteristics of wave–formed sand ripples [*Wiberg and Harris*, 1994]. In spite of the anisotropy of wave–formed sand ripples, the present measurements are not sufficient to reject a model in which the effective bottom roughness is independent of flow direction, although they do not necessarily preclude such a dependence.

Three conclusions result from our work. The first, supported by measurements during both glimpse 1 and glimpse 2, is that wave boundary layers with approximately the scale and structure expected on the basis of theoretical models and laboratory experiments occur under surface waves over rippled beds on oceanic sand beaches. The second conclusion, supported by measurements during glimpse 1 and equivocally by measurements during glimpse 2, is that the mean alongshore flow over a rippled sand beach has the qualitative distortion within the wave boundary layer that has previously been predicted theoretically and observed in laboratory measurements. The third conclusion is that waves and currents over sand beaches experience an effective bottom roughness that is approximately consistent with existing semiempirical representations of the roughness characteristics of wave–formed sand ripples.

Acknowledgments. This research was supported by the Coastal Sciences Program of the Office of Naval Research. We are grateful to Chuck Pottsmith, who was instrumental in designing and constructing the LDV system; to Sandy Williams for making a BASS sensor available for the purposes of our experiment; and to Janet Fredericks for her thorough processing, compilation, and preliminary evalution of the data. We also thank the staff of the U. S. Army Corps of Engineers Field Research Facility in Duck, North Carolina, including, in particular, Bill Birkemeier, for his support, encouragement, and hospitality, and Gene Bichener, for his facilitation of the deployment and recovery operations. This is contribution 9042 from the Woods Hole Oceanographic Institution.

References

Abramowitz, M., and I. A. Stegun, *Handbook of Mathematical Functions*, U. S. Department of Commerce, National Bureau of Standards, 1970.

Agrawal, Y. C. and D. G. Aubrey, Velocity observations above a rippled bed using laser–Doppler velocimetry, *J. Geophys. Res.*, *97*, 20,249–20,260, 1992.

Batchelor, G. K., *An Introduction to Fluid Dynamics*, Cambridge Univ. Press, New York, 1967.

Birkemeier, W. A., H. C. Miller, S. D. Wilhelm, A. D. DeWall, and C. S. Gorbics, A user's guide to the Coastal Engineering Research Center's (CERC's) Field Research Facility, *Instr. Rept. CERC–85–1*, 136 pp., U. S. Army Corps of Eng. Waterw. Exp. Stn., Coastal Eng. Res. Cent., Vicksburg, Miss., 1985.

Brevik, I., Oscillatory rough turbulent boundary layers, *J. Waterw. Port Coastal Ocean Div. Am. Soc. Civ. Eng.*, *107*, 175–188, 1981.

Conley, D., and D. L. Inman, Field observations of the fluid–granular boundary layer under near–breaking waves, *J. Geophys. Res.*, *97*, 9631–9644, 1992.

Dean, R. G., and R. A. Dalrymple, *Water Wave Mechanics for Engineers and Scientists*, 353 pp., Prentice–Hall, Englewood Cliffs, N. J., 1984.

Dick, J. E., and J. F. A. Sleath, Velocities and concentrations in oscillatory flow over beds of sediment, *J. Fluid Mech.*, *233*, 165–196, 1991.

Drake, D. E., D. A. Cacchione, and W. D. Grant, Shear stress and bed roughness estimates for combined wave and current flows over a rippled bed, *J. Geophys. Res.*, *97*, 2319–2326, 1992.

Draper, N. R., and H. Smith, *Applied Linear Regression*, John Wiley, New York, 1966.

DuToit, C. G., and J. F. A. Sleath, Velocity measurements close to rippled beds in oscillatory flow, *J. Fluid Mech.*, *112*, 71–96, 1981.

Fredericks, J. J., J. H. Trowbridge, and Y. C. Agrawal, Observations of near–bottom flow in a wave–dominated nearshore environment, *Tech. Rept. 94-04*, 124 pp., Woods Hole Oceanogr. Inst., Woods Hole, Mass., 1994.

Glenn, S. M., and W. D. Grant, A suspended sediment stratification correction for combined wave and current flows, *J. Geophys. Res.*, *92*, 8244–8264, 1987.

Grant, W. D., and O. S. Madsen, Combined wave and current interaction with a rough bottom, *J. Geophys. Res.*, *84*, 1797–1808, 1979.

Guza, R. T., and E. B. Thornton, Local and shoaled comparisons of sea surface elevations, pressures, and velocities, *J. Geophys. Res.*, *85*, 1524–1530, 1980.

Hara, T., and C. C. Mei, Oscillatory flows over periodic rigid ripples, *J. Fluid Mech. 211*, 183–209, 1989.

Hay, A. E., and J. Sheng, Vertical profiles of suspended sand concentration and size from multifrequency acoustic backscatter, *J. Geophys. Res.*, *97*, 15,661–15,678, 1992.

Hino, M., M. Kashiwayanagi, A. Nakayama, and T. Hara, Experiments on the turbulent statistics and the structure of a reciprocating oscillatory flow, *J. Fluid Mech.*, *131*, 363–400, 1983.

Jackson, P. S., On the displacement height in the logarithmic velocity profile, *J. Fluid Mech.*, *111*, 15–25, 1981.

Jensen, B. L., B. M. Sumer, and J. Fredsoe, Turbulent oscillatory boundary layers at high Reynolds numbers, *J. Fluid Mech.*, *206*, 265–298, 1989.

Jonsson, I. G., and N. A. Carlsen, Experimental and theoretical investigations in an oscillatory turbulent boundary layer, *J. Hydraul. Res.*, *14*, 45–60, 1976.

Kajiura, K., A model of the bottom boundary layer in water waves, *Bull. Earthquake Res. Inst.*, *46*, 75–123, 1968.

Kemp, P. H., and R. R. Simons, The interaction between waves and a turbulent current: Waves propagating with the current, *J. Fluid Mech.*, *116*, 227–250, 1982.

Kemp, P. H., and R. R. Simons, The interaction between waves and a turbulent current: Waves propagating against the current, *J. Fluid Mech.*, *130*, 73–89, 1983.

Longuet–Higgins, M. S., On the joint distribution of wave periods and amplitudes in a random wave field, *Proc. Rl. Soc. London, A 389*, 241–258, 1983.

Longuet–Higgins, M. S., Oscillating flow over steep sand ripples, *J. Fluid Mech.*, *107*, 1–35, 1981.

Madsen, O. S., Combined wave–current flows over a rippled bottom: Theoretical considerations (abstract), *Eos Trans. AGU 72*(44), Fall Meet. suppl., 299, 1991.

Monin, A. S., and A. M. Yaglom, *Statistical Fluid Mechanics*, 769 pp., MIT Press, Cambridge, Mass., 1971.

Nezu, I., and W. Rodi, Open–channel flow measurements with a laser Doppler anemometer, *J. Hydraul. Eng.*, *112*, 335–355, 1986.

Sato, S., M. Mimura, and A. Watanabe, Oscillatory boundary layer flow over rippled beds, in *Proceedings of the 19th Coastal Eng. Conf.*, *3*, 2293–2309, American Society of Civil Engineers, New York, 1984.

Sawamoto, M., and T. Yamashita, Sediment transport rate due to wave action, *J. Hydrosci. Hydraul. Eng.*, *4*, 1–15, 1986.

Sleath, J. F. A., Velocities above a rough bed in oscillatory flow, *J. Waterw. Port Coastal Ocean Div. Am. Soc. Civ. Eng.*, *100*, 287–304, 1974.

Sleath, J. F. A., Turbulent oscillatory flow over rough beds, *J. Fluid Mech.*, *182*, 369–410, 1987.

Sleath, J. F. A., Seabed boundary layers, in *The Sea*, vol. 9, *Ocean Engineering Science*, edited by B. Le Mehaute and D. M. Hanes, pp. 693–728, John Wiley, New York, 1990.

Smith, J. D., Modeling of sediment transport on continental shelves, in *The Sea*, vol. 6, *Marine Modelling*, edited by E. D. Goldberg, I. N. McCave, J. J. O'Brien, and J. H. Steele, pp. 539–577, John Wiley, New York, 1977.

Stauble, D. K., Long–term profile and sediment morphodynamics: Field Research Facility case history, *Tech. Rept. CERC–92–7*, 252 pp., U. S. Army Corps of Eng. Waterw. Exp. Stn., Coastal Eng. Res. Cent., Vicksburg, Miss., 1992.

Wiberg, P. L., and C. K. Harris, Ripple geometry in wave–dominated environments, *J. Geophys. Res.*, *99*, 775–789, 1994.

Williams, A. J., J. S. Tochko, R. L. Koehler, W. D. Grant, T. F. Gross, and C. V. R. Dunn, Measurement of turbulence in the oceanic bottom boundary layer with an acoustic current meter array, *J. Atmos. Oceanic Technol.*, *4*, 312–327, 1987.

J. H. Trowbridge, Woods Hole Oceanographic Institution, Woods Hole, MA 02543. (e-mail: jtrowbridge@whoi.edu)

Y. C. Agrawal, Sequoia Scientific, Incorporated, Mercer Island, WA 98040. (e-mail: yogi@zelda.nwra.com)

(Received July 22, 1994; revised March 24, 1995; accepted June 8, 1995.)